(12) INTERNATIONAL APPLICATION PUBLISHED UNDER THE PATENT COOPERATION TREATY (PCT)

(19) World Intellectual Property Organization
International Bureau

(43) International Publication Date
9 November 2006 (09.11.2006)

PCT

(10) International Publication Number
WO 2006/119475 A2

(51) International Patent Classification:
A61B 5/00 (2006.01)

(21) International Application Number:
PCT/US2006/017304

(22) International Filing Date: 4 May 2006 (04.05.2006)

(25) Filing Language: English

(26) Publication Language: English

(30) Priority Data:
60/677,770 4 May 2005 (04.05.2005) US

(71) Applicant *(for all designated States except US)*: **JOHNS HOPKINS UNIVERSITY** [US/US]; 5th Floor, 100 N. Charles Street, Baltimore, MD 21201 (US).

(72) Inventors; and

(75) Inventors/Applicants *(for US only)*: **PRINCE, Jerry L.** [US/US]; 20 Westminster Bridge Way, Lutherville, MD 21093 (US). **STUBER, Matthias** [CH/US]; 10171 Breconshire Road, Ellicott City, MD 21042 (US). **OSMAN, Nael Fakhry** [EG/US]; 1801 Rambling Ridge Lane #301, Baltimore, MD 21209 (US). **ABD-ELMONIEM, Khaled Zakarya** [EG/US]; 2933 N. Calvert Street #2F, Baltimore, MD 21218 (US).

(74) Agents: **RADHAKRISHNAN, Kanika** et al.; EVERGREEN VALLEY LAW GROUP P.C., 2675 S. White Road, Suite 275, San Jose, CA 95148 (US).

(81) Designated States *(unless otherwise indicated, for every kind of national protection available)*: AE, AG, AL, AM, AT, AU, AZ, BA, BB, BG, BR, BW, BY, BZ, CA, CH, CN, CO, CR, CU, CZ, DE, DK, DM, DZ, EC, EE, EG, ES, FI, GB, GD, GE, GH, GM, HR, HU, ID, IL, IN, IS, JP, KE, KG, KM, KN, KP, KR, KZ, LC, LK, LR, LS, LT, LU, LV, LY, MA, MD, MG, MK, MN, MW, MX, MZ, NA, NG, NI, NO, NZ, OM, PG, PH, PL, PT, RO, RU, SC, SD, SE, SG, SK, SL, SM, SY, TJ, TM, TN, TR, TT, TZ, UA, UG, US, UZ, VC, VN, YU, ZA, ZM, ZW.

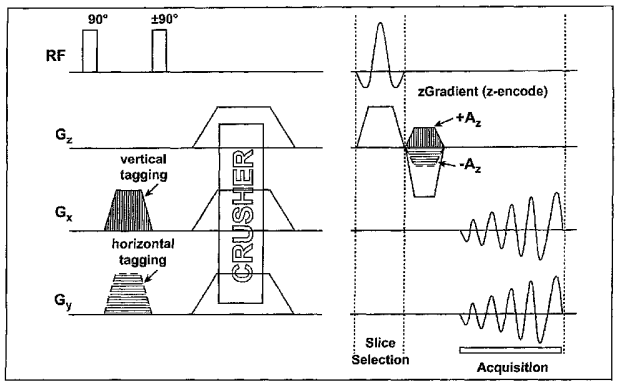
(84) Designated States *(unless otherwise indicated, for every kind of regional protection available)*: ARIPO (BW, GH, GM, KE, LS, MW, MZ, NA, SD, SL, SZ, TZ, UG, ZM, ZW), Eurasian (AM, AZ, BY, KG, KZ, MD, RU, TJ, TM), European (AT, BE, BG, CH, CY, CZ, DE, DK, EE, ES, FI, FR, GB, GR, HU, IE, IS, IT, LT, LU, LV, MC, NL, PL, PT, RO, SE, SI, SK, TR), OAPI (BF, BJ, CF, CG, CI, CM, GA, GN, GQ, GW, ML, MR, NE, SN, TD, TG).

Published:

— *without international search report and to be republished upon receipt of that report*

For two-letter codes and other abbreviations, refer to the "Guidance Notes on Codes and Abbreviations" appearing at the beginning of each regular issue of the PCT Gazette.

(54) **Title:** THREE DIMENSIONAL MAGNETIC RESONANCE MOTION ESTIMATION ON A SINGLE IMAGE PLANE



(57) **Abstract:** Three-dimensional MR motion estimation on a single image plane based on tagged MRI and HARP processing. Tagged magnetic resonance imaging technique encodes and automatically tracks displacement of spatially modulated object in three dimensions, encoding both in plane and through-plane motion in a single image plane without affecting acquisition speed. Post processing unravels encoding in order to directly track 3-D displacement of points within the image plane throughout image sequence. The invention is particularly suited to use on a heart for tracking and determining myocardial displacement. In one embodiment, an MR pulse sequence extends a slice following complementary spatial modulation of magnetization (CSPAMM) pulse sequence with two small z-encoding gradients immediately before the readouts in successive CSPAMM acquisitions, thereby adding a through-plane encoding from which through-plane motion can be computed from acquired images. HARP processing is used to determine in-plane motion, after which through-plane position can be determined using phase encodings. Use of balanced encodings and horizontal and vertical tags permits cancellation of systematic phase artifacts present in CSPAMM acquisitions.

WO 2006/119475 A2

THREE DIMENSIONAL MAGNETIC RESONANCE MOTION ESTIMATION ON A SINGLE IMAGE PLANE

BACKGROUND

Field

[0001] Invention relates generally to tagged magnetic resonance imaging, and in particular to three-dimensional quantification without long image acquisition times and user-intensive post-processing methods.

Related Art

[0002] The use of magnetic resonance imaging (MRI) for the quantification of regional function of the heart based on the measurement of motion has great potential for clinical adoption. However, the primary limiting factors to date are the lengthy image acquisition protocols and tedious post-processing procedures required to yield regional motion measures.

[0003] Three main MRI protocols that have been used for the quantification of myocardial motion are myocardial tagging, displacement encoding with stimulated echoes (DENSE), and phase contrast (PC) velocity encoding techniques. See, generally, Aletras et al., *"DENSE: Displacement Encoding with Stimulated Echoes,"* Cardiac Functional MRI. J. Magn. Reson. 173 (1999) 247-252; Aletras et al., *"Mixed echo train acquisition displacement encoding with stimulated echoes: an optimized DENSE method for in vivo functional imaging of the human heart,"* Magn. Reson. Med. 46 (2001) 523–534; Pelc et al., *"Phase contrast cine magnetic resonance imaging,"* Magn. Reson. Q. 7 (1991) 229-254, and Pelc et al., *"Quantitative magnetic resonance flow imaging,"* Magn. Reson. Q. 10 (1994) 125-147.

[0004] In tagging, myocardial spins are modulated at end-diastole in a pre-specified pattern. Later in the cardiac cycle, the displaced taglines are imaged and tracked using post-processing algorithms in order to compute displacement and strain images. This technique permits rapid imaging and visualization as well as fast, automatic computation of in-plane (i.e. two-dimensional) motion measures using harmonic phase (HARP) processing. See, generally, Osman et al., *"Cardiac Motion Tracking Using CINE Harmonic Phase (HARP) Magnetic Resonance Imaging,"* Magn. Reson. Med. 42(6) (1999) 1048–1060, and Osman et al., *"Imaging heart motion using harmonic phase*

MRI," IEEE Trans. Med. Imag., 19(3) (2000) 186–202. To date, however, there has been no extension to three dimensions in an equally efficient and automatic way.

[0005] Phase contrast imaging adds to every myocardial spin a phase value proportional to the velocity in the encoding direction. PC imaging times are generally long and phase distortion leads to significant measurement errors. Also, since velocity rather than displacement is the measured quantity, computation of displacement and strain (as opposed to strain rate) at later times in a sequence is typically corrupted by numerical integration errors. PC is readily extended to three dimensions though imaging time becomes prohibitively long.

[0006] DENSE encodes position in a manner similar to MR tagging through the use of stimulated echoes. Automatic processing analogous to HARP can then be used to compute displacement and strain. The acquisition protocol of DENSE supports higher spatial resolution than that of conventional HARP techniques, but the computation of in-plane motion is sensitive to through-plane motion in DENSE, unlike conventional tagging techniques.

[0007] To date, extension of these three basic approaches to three dimensions has required extensive additional data collection over that of 2-D imaging. Furthermore, except for PC, the results yield only sparse motion information. In all three cases, long imaging times may be prohibitive due to patient breath-holding constraints or may produce sub-optimal results due to gross mis-registration of images collected over a long period of time.

[0008] As a result, no practical fully three-dimensional approach to the imaging of regional cardiac function is available. Accordingly, a need exists for imaging techniques and processing methods that overcome these difficulties.

SUMMARY

[0009] The above-described need has been met by the present invention.

[0010] A method for three-dimensional MR motion estimation on a single image plane (hereinafter also referred to as *z*HARP) based on tagged MRI and HARP processing. Tagged magnetic resonance imaging technique encodes and automatically tracks displacement of spatially modulated object in three dimensions, encoding both in-plane and through-plane motion in a single image plane without affecting acquisition speed. Post-processing unravels encoding in order to directly track 3-D displacement of points

within the image plane throughout image sequence. The invention is particularly suited to use on a heart for tracking and determining myocardial displacement.

[0011] In one embodiment, an MR pulse sequence extends a slice-following complementary spatial modulation of magnetization (CSPAMM) pulse sequence with two small *z*-encoding gradients immediately before the readouts in successive CSPAMM acquisitions, thereby adding a through-plane encoding from which through-plane motion can be computed from acquired images. HARP processing is used to determine in-plane motion, after which through-plane position can be determined using phase encodings. Use of balanced encodings and horizontal and vertical tags permits cancellation of systematic phase artifacts present in CSPAMM acquisitions.

[0012] In another embodiment, a pulse sequence based on cosine and sine modulation to eliminate (CANSEL) artifact-generating echoes is used to obtain complete acquisition of *z*HARP data from an isolated spectral peak in five acquisitions, allowing artifact-free 3-D point tracking without phase mapping.

[0013] When used in a single image plane, *z*HARP yields a dense three-dimensional motion map of points in the plane and can be used to compute surface strain. When used with multiple image planes, *z*HARP tracks a rich collection of points within the myocardium and allows computation of fully 3-D measures of regional function, such as radial, circumferential, and longitudinal strain and twist, principal strains, or the direction of maximal thickening. *Z*HARP can also be used to compute a 3-D measure of global function, such as longitudinal shortening, rotation, or torsion.

[0014] It is an object of the present invention to compute dense 3-D motion from a single acquired image orientation without incurring an increase in imaging time over that of slice following CSPAMM.

[0015] It is a further object of the present invention to show consistent tracking performance throughout the time of tag persistence, in contract to the PC method where tracking errors accumulate over time.

[0016] It is a further object of the present invention to between in-plane strain and 3-D rotation, resolving an inherent ambiguity in 2-D HARP which cannot differentiate between in-plane strain and a simple 3-D rotation.

[0017] These and other objects of the invention will be more fully understood from the following description of the invention with reference to the drawings appended hereto.

BRIEF DESCRIPTION OF DRAWINGS

[0018] Fig. 1 illustrates a zHARP pulse sequence.

[0019] Fig. 2 illustrates extraction of displacement-encoding phase maps.

[0020] Fig. 3 illustrates short axis (SA) and long axis (LA) slice orientations for an experiment described in the first example below.

[0021] Fig. 4 illustrates displacement phase maps extraction for the experiment described in the first example below.

[0022] Fig. 5 illustrates *z* displacement maps extraction for the experiment described in the first example below.

[0023] Fig. 6 illustrates *z* displacement profile in the first 460ms of a phantom motion cycle for the experiment described in the first example below.

[0024] Fig. 7 illustrates short axis (SA) and long axis (LA) slice orientations for the experiment described in the second example below.

[0025] Fig. 8 shows the displacement profile through a motion cycle for the experiment described in the second example below.

[0026] Fig. 9 illustrates tracking results of sample time-frames for the experiment described in the second example below.

[0027] Fig. 10 illustrates data used in the experiment described in the third example below.

[0028] Fig. 11 illustrates a mesh tracking result, with in-plane displacements shown as twisting and binding of the mesh grid lines, and through-plane displacement shown as colors of the points.

[0029] Fig. 12 illustrates *z* displacement tracking results for points around the myocardium for the experiment described in the third example below.

[0030] Fig. 13 illustrates an example of false apparent strain due to through-plane motion.

[0031] Fig. 14 illustrates some images acquired using the cylindrical phantom experiment described in the fourth example below.

[0032] Fig. 15 illustrates the regional strain profiles within the phantom experiment described in the fourth example below.

[0033] Fig. 16 illustrates results obtained in a healthy adult subject as described in the fourth example below.

DETAILED DESCRIPTION

[0034] As employed herein, the term "patient" shall mean a living member of the animal kingdom including human beings.

[0035] As employed herein, the term "object" shall mean a portion of a patient which is the subject of dynamic motion with respect to other portions of the body or with respect to the surroundings of the body and shall expressly include, but not be limited to, the heart and portions thereof, muscles, tongue, cerebrospinal fluid, and the brain.

[0036] Tagged MRI uses an MR scanner to temporarily change the magnetic properties in and around the heart in a pre-specified pattern, which can the be imaged as both the heart and the pattern undergo deformation. Analysis of the deformed patterns in the resulting image sequence yields information about the motion of the heart muscle within its walls.

[0037] The present invention (*z*HARP) discloses MRI techniques for imaging and automatically tracking the 3-D displacement of points in an image plane, such as myocardial points. A pulse sequence for acquiring an image that encodes both in-plane and through-plane motion without affecting the acquisition speed of the underlying pulse sequence is presented. Also presented are methods, based on the harmonic phase (HARP) concept, which track the 3-D displacements of points in the image plane through the image sequence. The presented methodology is validated in both phantom and human studies.

Pulse sequence

[0038] To measure the motion of an object by magnetic resonance imaging, a region of interest in the object is spatially modulated using a slice-following 3-D tagging imaging sequence (pulse sequence). The pulse sequence used in the present invention is based on a standard slice-following CSPAMM (SF-CSPAMM) sequence (see, generally, Fischer et al., *"True Myocardial Motion Tracking,"* Magn. Reson. Med. 31 (1994) 401) but with the addition of a *z*-encoding gradient applied twice before the read-out to the second orthogonal CSPAMM acquisition, wherein the *z*-encoding gradient is applied with opposite polarity the second time around.

[0039] Fig. 1 illustrates a *z*HARP pulse sequence, showing a typical CSPAMM tagging spiral acquisition sequence with an added *z*-encode gradient with magnitude $|A_z|$ in the slice-select direction. A $+A_z$ gradient and a $-A_z$ gradient are added to vertical and horizontal tagging sequences, respectively. The gradient adds a *z*-position dependent

phase φ_z to material points in an acquired slice. This additional phase is linearly related to the distance of the point from the isocenter of the scanner. While susceptibility and general field inhomogeneities lead to an additional (artifactual) phase accumulation φ_e, this erroneous phase is identical in both the horizontally and vertically tagged images and will be shown to (mathematically) vanish in the computation of in-plane and through-plane displacements.

ZHARP Formulation

[0040] The zHARP z-encode gradient has the same strength for A and B CSPAMM acquisitions. Upon complex signal acquisition and subtraction, the signal from the untagged tissue is removed, similar to standard CSPAMM. However, the tagged tissue now has a z-phase, acquired at the imaging moment. Accordingly, the z-encoded CSPAMM image $I(r,t)$ at $r(x,y)$ and time t can be represented as

[0041] $$I(r,t) = 2\int_{\bar{z}(\mathrm{r})-\Delta/2}^{\bar{z}(\mathrm{r})+\Delta/2} \rho(\mathrm{r},t) e^{j\varphi_e(\mathrm{r})} \cos(\omega^{\mathrm{T}} \mathrm{p}(\mathrm{r},t)) e^{j\kappa_z(\mathrm{r})z(\mathrm{r})} dz \qquad (1)$$

[0042] wherein $\bar{z}$ is the (tag) slice position, Δ is the (tag) slice thickness, $\rho(\mathrm{r},t)$ is the effective spin density, ω is the tag frequency, $\mathrm{p}(\mathrm{r},t)$ is the reference map (the position of the 3-D spatial point r at the reference time), and κ_z is the z-encode frequency.

[0043] If the frequency κ_z is small enough and the slice thin enough, we obtain the approximation

[0044] $$I(\mathrm{r},t) \approx 2\rho(\mathrm{r},t) e^{j\varphi_e(\mathrm{r})} \cos(\omega^{\mathrm{T}} \mathrm{p}(\mathrm{r},t)) e^{j\kappa_z(\mathrm{r})\bar{z}(\mathrm{r})} \qquad (2)$$

[0045] Letting $\varphi_z(\mathrm{r}) = \kappa_z(\mathrm{r})\bar{z}(\mathrm{r})$, (2) becomes

[0046] $$I(\mathrm{r},t) \approx 2\rho(\mathrm{r},t) e^{j\varphi_e(\mathrm{r})} e^{j\varphi_z(\mathrm{r})} \cos(\omega^{\mathrm{T}} \mathrm{p}(\mathrm{r},t)). \qquad (3)$$

[0047] This is the commonly known CSPAMM image multiplied by $e^{j\varphi_e(\mathrm{r})} e^{j\varphi_z(\mathrm{r})}$, which means that the $\bar{z}$ positions of myocardial material points in the slice are now encoded in the phase of the complex image I without affecting the usual CSPAMM magnitude content. For simplicity of notation in the following, we omit the argument of $\varphi_e(\mathrm{r})$ and $\varphi_z(\mathrm{r})$.

ZHARP Images

[0048] An image plane is scanned twice in order to compute the in-plane motion, first with vertical tagging $\omega = \omega_x(1,0,0)$, and then with horizontal tagging $\omega = \omega_y(0,1,0)$. A

positive z-encode gradient is applied to the first scan and a negative z-encode gradient is applied to the second scan. Using the relation

[0049] $\mathrm{p}(\mathrm{r},t) = r - \mathrm{u}(\mathrm{r},t)$, (4)

[0050] wherein u is the displacement, (3) becomes

[0051] $I_x(\mathrm{r},t) \propto \rho(\mathrm{r},t)e^{j\varphi_e}e^{j\varphi_z}\cos(\omega_x x - \varphi_x)$, (5)

[0052] $I_y(\mathrm{r},t) \propto \rho(\mathrm{r},t)e^{j\varphi_e}e^{-j\varphi_z}\cos(\omega_y y - \varphi_y)$, (6)

[0053] for the first and second scans, wherein $\varphi_x = \omega_x u_x$ and $\varphi_y = \omega_y u_y$. In these equations, the phases φ_x and φ_y are called either the displacement-encoding phases or the harmonic phase (HARP) maps in the x and y directions, respectively. See, generally, Osman et al, *"Imaging heart motion using harmonic phase MRI,"* IEEE Trans. Med. Imag., 19(3)(2000)186–202. It is noted that grid tags may be used as well, in which case they may have both the vertical and horizontal tags and the acquired images will be grid tagged images. The grid tagged images may be vertically and horizontally tagged, or they may be tagged in any two orthogonal directions.

[0054] Two steps are used to extract the 3-D displacement of a material point.

[0055] **Step 1: Extraction of displacement-encoding phase maps.** Although at first glance it may appear impossible to sort out the in-plane and through-plane motion components from the image data in (5) and (6), it can nevertheless be accomplished by applying the 2-D HARP concept (see, generally, Osman et al, *"Imaging heart motion using harmonic phase MRI,"* IEEE Trans. Med. Imag., 19(3)(2000)186–202, and Osman et al., *"Cardiac Motion Tracking Using CINE Harmonic Phase (HARP) Magnetic Resonance Imaging,"* Magn. Reson. Med. 42(6)(1999)1048–1060) to the negative and positive harmonic peaks of I_x and I_y. This idea is illustrated in the block diagram of Fig. 2. Whereas in conventional HARP there would be only two harmonic phases that are computed, one for the horizontally tagged image and one for the vertically tagged image, the present invention computes four harmonic phases, ϕ_A, ϕ_B, ϕ_C, and ϕ_D. Furthermore, these computed phases include not only the harmonic phases, φ_x and φ_y arising from object in-plane motion, but also a phase φ_z arising from the explicit z-encoding and a phase φ_e arising from erroneous phase sources.

[0056] Fig. 2 illustrates extraction of displacement-encoding phase maps, with the left flowchart showing the extraction of ϕ_A and ϕ_B of from vertically tagged images I_x, and

the right flowchart showing the extraction of ϕ_C and ϕ_D of from horizontally tagged images I_y. The $*$ and δ symbols represent linear convolution and the impulse function, respectively. The computed harmonic phases form the following system of linear equations:

[0057] $\phi_A = \varphi_e + \varphi_z - \varphi_x$, (7)

[0058] $\phi_B = \varphi_e + \varphi_z + \varphi_x$, (8)

[0059] $\phi_C = \varphi_e - \varphi_z - \varphi_y$, (9)

[0060] $\phi_D = \varphi_e - \varphi_z + \varphi_y$. (10)

[0061] This system is readily solved for the desired phases that are related to motion, yielding

[0062] $\varphi_x = (\phi_B - \phi_A)/2$, (11)

[0063] $\varphi_y = (\phi_D - \phi_C)/2$, (12)

[0064] $\varphi_z = ((\phi_A - \phi_B) - (\phi_C - \phi_D))/4$. (13)

[0065] Step 2: 3-D Motion Tracking. Consider a material point located at r_m at time t_m. The principle of 2-D HARP tracking (see, generally, Osman et al., *"Cardiac Motion Tracking Using CINE Harmonic Phase (HARP) Magnetic Resonance Imaging,"* Magn. Reson. Med. 42(6)(1999)1048–1060) is based on the fact that HARP phase is a material property, and therefore that the apparent in-plane position of this point at time t_{m+1}, given by r_{m+1}, can be determined by the following relations:

[0066] $\varphi_x(\mathrm{r}_{m+1}, t_{m+1}) = \varphi_x(\mathrm{r}_m, t_m)$, (14)

[0067] $\varphi_y(\mathrm{r}_{m+1}, t_{m+1}) = \varphi_y(\mathrm{r}_m, t_m)$. (15)

[0068] Now consider a point on the image plane r_0 at the time t_0 of tag application. Since the phases φ_x and φ_y are found using (11) and (12), 2-D HARP tracking can be used to track the apparent in-plane position of r_0 throughout the image sequence (see, generally, Osman et al, *"Imaging heart motion using harmonic phase MRI,"* IEEE Trans. Med. Imag., 19(3)(2000)186–202). This yields a sequence of points in the image plane given by $\{\mathrm{r}_0, \mathrm{K}, \mathrm{r}_m, \mathrm{r}_{m+1}, \mathrm{K}\}$. This is a standard HARP result, a tracking of the apparent 2-D position of an arbitrary point in the plane. Advantageously, using the present

invention this result can be obtained despite the presence of an explicit *z*-encode and the presence of phase anomalies.

[0069] Because slice following is used, it is now possible to recover the *z* position of r_0 throughout the sequence. At the time of tag (and *z*-encode) application, we have

[0070] $$\varphi_z(r_0,t_0) \approx \kappa_z z_0. \quad (16)$$

[0071] At a later time, if the *z* phase does not wrap, we have the relation

[0072] $$\varphi_z(r_{m+1},t_{m+1}) - \varphi_z(r_m,t_m) \approx \kappa_z(z_{m+1} - z_m). \quad (17)$$

[0073] Rearranging, and using the wrapping operator W as defined in above-referenced Osman et al, *"Imaging heart motion using harmonic phase MRI"* (which recovers the correct net phase difference), yields

[0074] $$z_{0+1} = z_0 + \frac{1}{\kappa_z} W\{\varphi_z(r_{m+1},t_{m+1}) - \varphi_z(r_m,t_m)\}, \quad (18)$$

which can be used in an iterative fashion to track the *z* position of r_0 throughout the sequence.

[0075] Together, the above two steps describe the algorithmic component of *z*HARP. It should be obvious to one of ordinary skill in the art that a single point or an arbitrary collection of points in an image slice can be tracked in three dimensions using this imaging and processing methodology.

[0076] In another embodiment, a pulse sequence based on cosine and sine modulation to eliminate (CANSEL) artifact-generating echoes is used to obtain complete acquisition of *z*HARP data from an isolated spectral peak in five acquisitions, allowing artifact-free 3-D point tracking without phase mapping.

[0077] In order to confirm the effectiveness of the methods of the present invention, experiments were performed on phantoms and a normal human volunteer. Quantitative comparisons between *z*HARP and prior art tag tracking methods are made.

Example 1: 1-D *z* displacement of phantom

[0078] The pulse sequence and the algorithm were tested on a water-filled-bottle phantom moving sinusoidally (1" peak-to-peak) in parallel to the main magnetic field (*z* direction) at a rate of 52 cpm. The orientations of the acquired slice, so-called short axis (SA) slice, as well as the long axis (LA) slice are shown in Fig. 3. Motion is along the B_0 field of the magnet. SA slice is along the bottle axis of symmetry and perpendicular to the direction of motion. LA slice is perpendicular to axis of symmetry. Fourteen axial-plane

cardiac phases were acquired during the first 466 ms of each cycle. Fig. 4 shows the *z*HARP algorithm steps applied to the 14th frame and how the through-plane and in-plane displacements were extracted. In this experiment, though-plane displacement occurred and was measured. Phase maps are shown at a rectangular region of interest (ROI) in the middle of the bottle. The magnitude image of the bottle is shown in the background of the ROI.

[0079] For comparison, the phantom was also imaged using a conventional PC method and a *z* displacement map was obtained thereafter by integration. Fig. 5 illustrates *z* displacement (φ_z) maps extraction for the experiment through the 14 CINE images, wherein t represents time, d represents displacement, and column (a) on the left shows maps using *z*HARP and on the right shows maps using PC. As a reference standard, *z* displacement was also computed using a cross correlation (CC) method applied to the LA tagged dataset, and column (b) shows a reference standard dataset with tagged long axis slices used for displacement calculations using the CC method.

[0080] Through-plane motion in the SA slice is shown as in-plane horizontal shift in the LA slice as shown in Fig.5. Fig.6 compares the mean displacement value and the standard deviation obtained from PC, *z*HARP, and CC. Relative RMS error between PC and CC was 10.7% and between *z*HARP and CC was only 4.0%. Fig. 6 shows the *z* displacement (φ_z) profile in the first 460ms of the phantom motion cycle, with graph (a) showing the displacement using *z*HARP and graph (b) showing displacement using PC, illustrating increasing standard deviation and drift of the PC values from the cross correlation values.

Example 2: 2-D combined *x* and *z* displacement

[0081] In the second experiment, the phantom and the imaged slice were tilted by 43° about the anterior-posterior axis while the phantom was moving along the B_0 field direction. In addition, a stationary water phantom was inserted above the imaging coil for comparison. In this tilted placement, both in-plane *x* displacement and through-plane *z* motion components were generated. Fig. 7 illustrates short axis (SA) and long axis (LA) slice orientations for the experiment.

[0082] Fig. 8 shows the displacement profile through a motion cycle, illustrating average in-plane and through-plane displacement profiles with time and the total 1" peak-to-peak displacement. Both *x* and *z* displacement maps are shown and, as expected, both displacements follow a sinusoidal pattern. Because of the tilting-setup,

$|\text{mean}(x\,\text{displacement})| = \tan(43°) \times |\text{mean}(z\,\text{displacement})|$ at any time. The total displacement profile $\sqrt{|z-\text{displacement}|^2 + |x-\text{displacement}|^2}$ is shown with 1" peak-to-peak total displacement as expected.

[0083] A rectangular mesh of points was constructed over the stationary and moving phantoms and tracked throughout the cycle. Tracking results of sample time-frames are shown in Fig. 9 illustrating SA CINE time-frames and tracking. The left shows sample tagged images at different time instants of the motion cycle (notice the horizontal motion of the phantom). The middle shows the corresponding *z*HARP mesh tracking, with in-plane tracking shown as a shift in the phantom position from frame to frame and through-plane tracking shown as a change in coloring. The right shows the color palette used for representing through-plane motion tracking.

[0084] The frames show both an SA slice in the moving phantom (in the center of the image) and a part of the stationary phantom (at the bottom of the image). Notice the yellow color of the stationary phantom and the change of the moving phantom from yellow ($z = 0$) to green ($z = -ve$) then to red ($z = +ve$) then to green ($z = -ve$) (compare with the profile in Fig. 8).

Example 3: Normal volunteer

[0085] The following data was obtained from a 26-year-old healthy adult male subject with a heart rate of approximately 80bpm. Four ECG leads were placed on the chest for triggering of the pulse sequence by the R-wave. The patient position was head first and supine. An oblique, equatorial short-axis, 6mm-thick slice of the left ventricle was scouted. Fig. 10(a) shows the location and orientation of a four-chambers slice (4C). The line shown is the intersection between the shown 4C and the acquired SA slice. Twelve systolic images of size 256×256 were acquired starting from end-diastole to end-systole with a square FOV of 35cm and temporal resolution of 30ms. The first and last time-frames were scanned 11ms and 341ms, respectively, after the R-wave trigger. Fig. 10(b) shows the twelve 97×97 LV region-of-interest (ROI) datasets as they appear in the acquired horizontal tag *z*HARP.

[0086] A 97×97 mesh of points was tracked on the ROI data. Results in Fig. 11 show in-plane twisting of the mesh and color-encoded *z* displacement. Fig. 12 shows the though-plane displacement profile of selected tracked points around the LV myocardium, with vertical axes in mm and horizontal axes representing the time-frame index.

[0087] Combining the techniques of the present invention with a multi-slice acquisition provides a layer-cake of 3-D tracked points which can be used to track the heart and compute a variety of strains, thereby allowing to significantly reduce the number of planes that are acquired, and still obtain an accurate assessment of the state of the LV and RV myocardium.

Resolving Through-plane Rotation Ambiguity

[0088] It is a further advantage of the present invention that it resolves an inherent ambiguity in 2-D HARP that prevents differentiating between an in-plane strain and a simple 3-D rotation. When quantitative strain maps are calculated for a cardiac imaging plane after an image slice is acquired using functional cardiac MRI methods, such as tagging (see, generally, Axel et al., *"Heart wall motion: improved method of spatial modulation of magnetization for MRI,"* Radiology 1989; 172:349–350), displacement encoding (see, generally, Pelc et al., *"Tracking of cyclic motion with phase-contrast cine MR velocity data"*, J Magn Reson Imaging 1995 May-Jun; 5(3):339-45), or velocity encoding (see, generally, Aletras et al, *"DENSE: displacement encoding with stimulated echoes in cardiac functional MRI,"* J Magn Reson. 1999 Mar; 137(1):247-52.), as a result of through-plane motion the imaged slice may not necessarily be the same slice that was motion-encoded, which may cause the computed strain to be inaccurate. With slice-following tagging (see, generally, Fischer et al., *"True myocardial motion tracking,"* Magn Reson Med. 1994 Apr; 31(4):401-13), the same tissue of the myocardium is always examined. However, through-plane rotation can still be misinterpreted as a false strain. As a result, only the in-plane motion and apparent strain can be computed when only a single slice is imaged. In contrast, the method of the present invention provides a true planar strain map for a given imaged slice by taking the through-plane motion into consideration and correcting for the false strain component caused by through-plane rotation.

[0089] As described above, *z*HARP images and automatically tracks the 3-D myocardial displacement of points in an image plane. *Z*HARP surpasses SF-CSPAMM, which only acquires the projection of a slice and implies that only in-plane x- and y-displacements can be obtained. An R-wave triggered tagged cardiac slice starts as a flat plane, undergoes in-plane and through-plane displacements and becomes a 3-D surface. As shown in Fig. 13, a through-plane rotation will be interpreted as in-plane compression when only x- and y-displacements are observed. With acquisition of the 3-D displacement components, this

misinterpretation of rotation is removed and a true planar strain map is obtained by using a 3x3 displacement gradient tensor instead of a 2x2 tensor. Given a slice acquired through an object such as the myocardium, the strain tensor at a material point is defined by:

[0100] $$e = \frac{1}{2}\left[\nabla_{\underline{x}}\underline{u} + (\nabla_{\underline{x}}\underline{u})^T\right] + \frac{1}{2}\left[(\nabla_{\underline{x}}\underline{u})^T \times (\nabla_{\underline{x}}\underline{u})\right] \quad (19)$$

[0101] where $\underline{u}(\underline{x}) = \underline{u}(x,y,z) = \begin{bmatrix} u_x \\ u_y \\ u_z \end{bmatrix}$ and $\nabla_{\underline{x}}\underline{u} = \begin{pmatrix} \frac{\partial u_x}{\partial x} & \frac{\partial u_x}{\partial y} & \frac{\partial u_x}{\partial z} \\ \frac{\partial u_y}{\partial x} & \frac{\partial u_y}{\partial y} & \frac{\partial u_y}{\partial z} \\ \frac{\partial u_z}{\partial x} & \frac{\partial u_z}{\partial y} & \frac{\partial u_z}{\partial z} \end{pmatrix}$.

[0102] Compared to SF-CSPAMM, *z*HARP acquires u_z in addition to u_x and u_y, wherein the component u_z is used to remove the false apparent strain due to through-plane rotation. With *z*HARP, this is done by adding u_z into the computation of the displacement gradient as follows:

[0103] $$\nabla_{\underline{x}}\underline{u} = \begin{pmatrix} \frac{\partial u_x}{\partial x} & \frac{\partial u_x}{\partial y} & 0 \\ \frac{\partial u_y}{\partial x} & \frac{\partial u_y}{\partial y} & 0 \\ \frac{\partial u_z}{\partial x} & \frac{\partial u_z}{\partial y} & 0 \end{pmatrix}, \quad (20)$$

[0104] in contrast to using

[0105] $$\nabla_{\underline{x}}\underline{u} = \begin{pmatrix} \frac{\partial u_x}{\partial x} & \frac{\partial u_x}{\partial y} \\ \frac{\partial u_y}{\partial x} & \frac{\partial u_y}{\partial y} \end{pmatrix}$$

with SF-SPAMM, wherein no u_z is acquired.

[0106] In order to confirm the effectiveness of the method for removing the through-plane rotation effect from the strain maps, phantom and in-vivo experiments were performed and are presented herein.

Example 4: Removing through-plane rotation effect from strain maps

[0107] The pulse sequence and methodology were tested first in a rotating gel-phantom experiment with 10ms acquisition window, 20 spirals, resolution = 256x256, FOV = 320mm, slice thickness = 8mm, tag spacing = 8mm, TE = 1.1ms, TR = 30ms. The

phantom was moving forward and backward in a direction parallel to the main magnetic field at a rate of 30rpm. Simultaneously, the phantom was rotating around its axis of symmetry as shown in Fig. 14. Fig. 14 illustrates some images acquired using this experimental setup. For in-vivo validation, a healthy 26-year-old male was scanned with 15ms acquisition window, 12 spirals, FOV = 350mm, slice thickness = 6mm, TE = 4ms. One SA and two LA slices were acquired. The intersection lines between the slices were obtained and tracked in 3-D (see Fig. 15), using 3D-SF-HARP (see, generally, Sampath et al., *"3D Tracking of Cardiac Material Points Using a Combined Slice-Following Harmonic Phase (SF-HARP) Magnetic Resonance Imaging Approach,"* Proc Intl Soc Magn Res Med (ISMRM), 2004), through-plane rotations φ of the lines were computed, and the expected false strain was obtained using the formula $\varepsilon = \cos(\varphi) - 1$.

[0108] Fig. 15 visualizes the regional strain profiles within the phantom in four different quadrants. Without removing the through-plane rotation effect, a false compression is detected. Results show the effective removal of through-plane rotation effect using the new method of the present invention. Fig. 16 shows results obtained in a healthy adult subject. A short axis slice is shown and is divided into eight segments. A dense mesh of points was tracked. Results show radial (Err) and circumferential (Ecc) before and after correction.

[0109] As a result, the presented planar strain mapping methodology resolves the strain ambiguity caused by through-plane rotation. With *z*HARP, the 3-D quantification of myocardial motion is obtained for an arbitrary slice with no extra scanning time, and by using these data and expanding the displacement gradient into 3-D, true planar strain can be computed for the imaged slice. When compared to conventional strain maps, a more accurate strain computation is observed.

[0110] All cited documents, including patents, patent applications, and other publications are incorporated herein by reference in their entirety.

[0111] Foregoing described embodiments of the invention are provided as illustrations and descriptions. They are not intended to limit the invention to precise form described. Other variations and embodiments are possible in light of above teachings, and it is thus intended that the scope of invention not be limited by this Detailed Description, but rather by Claims following.

CLAIMS

WE CLAIM:

1. A method of measuring three-dimensional motion of an object by magnetic resonance imaging from one acquired image orientation, comprising:

applying a magnetic resonance imaging pulse sequence to spatially modulate a region of interest of said object, the pulse sequence comprising a slice-following CSPAMM (complementary spatial modulation of magnetization) pulse sequence with added *z*-phase encode;

acquiring a set of one or more vertically tagged images and a set of one or more horizontally tagged images of said spatially modulated object; and

determining in-plane and through-plane motions of said spatially modulated object from the vertically and horizontally tagged images.

2. The method of Claim 1, wherein the pulse sequence comprises a vertical tagging sequence having a first *z*-encoding gradient and a horizontal tagging sequence having a second *z*-encoding gradient of equal magnitude but opposite polarity, thereby adding through-plane encoding from which through-plane motion can be computed from the acquired images.

3. The method of Claim 2, the determining including computing a first two harmonic phase images for a vertically tagged image and a second two harmonic phase images for a horizontally tagged image.

4. The method of Claim 3, the determining further including solving a system of linear equations at a set of image coordinates for phase images indicating in-plane and through-plane motion, the system of linear equations formed by the four harmonic phase images computed for the vertically and horizontally tagged images.

5. The method of Claim 4, the determining further including applying harmonic phase (HARP) processing to compute in-plane motion of said spatially modulated object.

6. The method of Claim 5, the determining further including iterative application of a wrapping operator to compute through-plane motion of said spatially modulated object.

7. The method of Claim 1, including employing said method to obtain a real-time image of cardiac motion.

8. The method of Claim 1, including employing said method to obtain a real-time image of myocardial strain.

9. The method of Claim 1, including employing said method to obtain a dense three-dimensional motion map of points in a plane for computing myocardial surface strain.

10. The method of Claim 1, including employing said method with a plurality of image planes to track a set of points within the myocardium for computing a three-dimensional measure of a regional function and global function.

11. The method of Claim 10, wherein the regional function comprises radial, circumferential, or longitudinal strain, principal strains, or the direction of maximal thickening.

12. The method of Claim 10, wherein global function comprises longitudinal shortening, rotation, or torsion.

13. The method of Claim 1, including employing said method to differentiate between in-plane strain and three-dimensional rotation, further comprising:

using a 3x3 displacement gradient tensor to remove an apparent false strain due to through-plane rotation; and

computing a planar strain within the imaged slice.

14. A method of measuring three-dimensional motion of an object by magnetic resonance imaging from one acquired image orientation, comprising:

applying a magnetic resonance imaging pulse sequence to spatially modulate a region of interest of said object, the pulse sequence comprising a slice-following CSPAMM (complementary spatial modulation of magnetization) pulse sequence with added *z*-phase encode;

acquiring a set of one or more of grid tagged images of said spatially modulated object; and

determining in-plane and through-plane motions of said spatially modulated object from the grid tagged images.

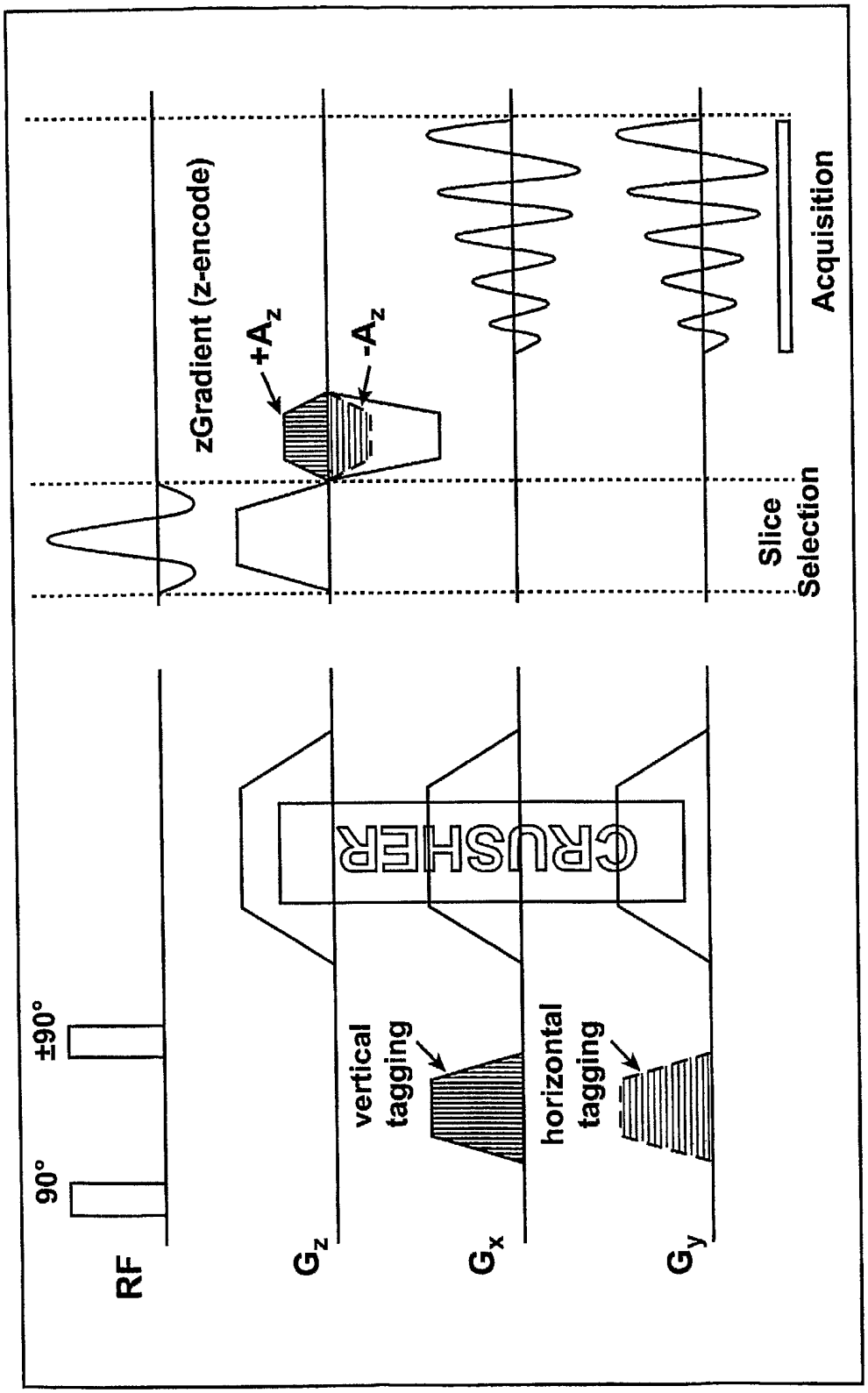

RF
90°
±90°
G_z
G_x
G_y
CRUSHER
vertical tagging
horizontal tagging
zGradient (z-encode)
+A_z
-A_z
Slice Selection
Acquisition

FIG. 1

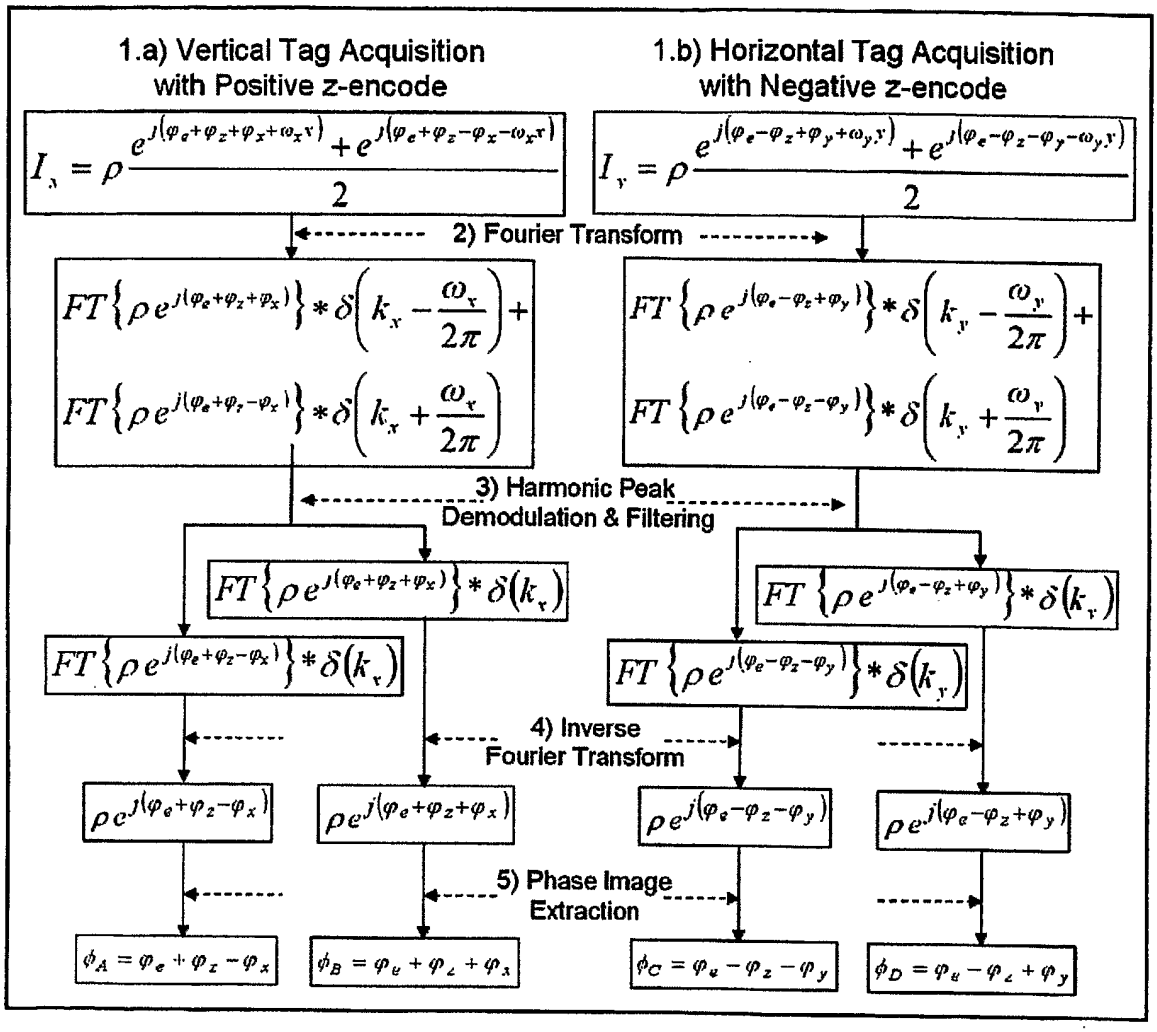

1.a) Vertical Tag Acquisition with Positive z-encode
1.b) Horizontal Tag Acquisition with Negative z-encode
$I_x = \rho \frac{e^{j(\varphi_e+\varphi_z+\varphi_x+\omega_x x)} + e^{j(\varphi_e+\varphi_z-\varphi_x-\omega_x x)}}{2}$
$I_y = \rho \frac{e^{j(\varphi_e-\varphi_z+\varphi_y+\omega_y y)} + e^{j(\varphi_e-\varphi_z-\varphi_y-\omega_y y)}}{2}$
2) Fourier Transform
$FT\left\{\rho e^{j(\varphi_e+\varphi_z+\varphi_x)}\right\} * \delta\left(k_x - \frac{\omega_x}{2\pi}\right) +$
$FT\left\{\rho e^{j(\varphi_e+\varphi_z-\varphi_x)}\right\} * \delta\left(k_x + \frac{\omega_x}{2\pi}\right)$
$FT\left\{\rho e^{j(\varphi_e-\varphi_z+\varphi_y)}\right\} * \delta\left(k_y - \frac{\omega_y}{2\pi}\right) +$
$FT\left\{\rho e^{j(\varphi_e-\varphi_z-\varphi_y)}\right\} * \delta\left(k_y + \frac{\omega_y}{2\pi}\right)$
3) Harmonic Peak Demodulation & Filtering
$FT\left\{\rho e^{j(\varphi_e+\varphi_z+\varphi_x)}\right\} * \delta(k_x)$
$FT\left\{\rho e^{j(\varphi_e+\varphi_z-\varphi_x)}\right\} * \delta(k_x)$
$FT\left\{\rho e^{j(\varphi_e-\varphi_z+\varphi_y)}\right\} * \delta(k_y)$
$FT\left\{\rho e^{j(\varphi_e-\varphi_z-\varphi_y)}\right\} * \delta(k_y)$
4) Inverse Fourier Transform
$\rho e^{j(\varphi_e+\varphi_z-\varphi_x)}$
$\rho e^{j(\varphi_e+\varphi_z+\varphi_x)}$
$\rho e^{j(\varphi_e-\varphi_z-\varphi_y)}$
$\rho e^{j(\varphi_e-\varphi_z+\varphi_y)}$
5) Phase Image Extraction
$\phi_A = \varphi_e + \varphi_z - \varphi_x$
$\phi_B = \varphi_e + \varphi_z + \varphi_x$
$\phi_C = \varphi_e - \varphi_z - \varphi_y$
$\phi_D = \varphi_e - \varphi_z + \varphi_y$

FIG. 2

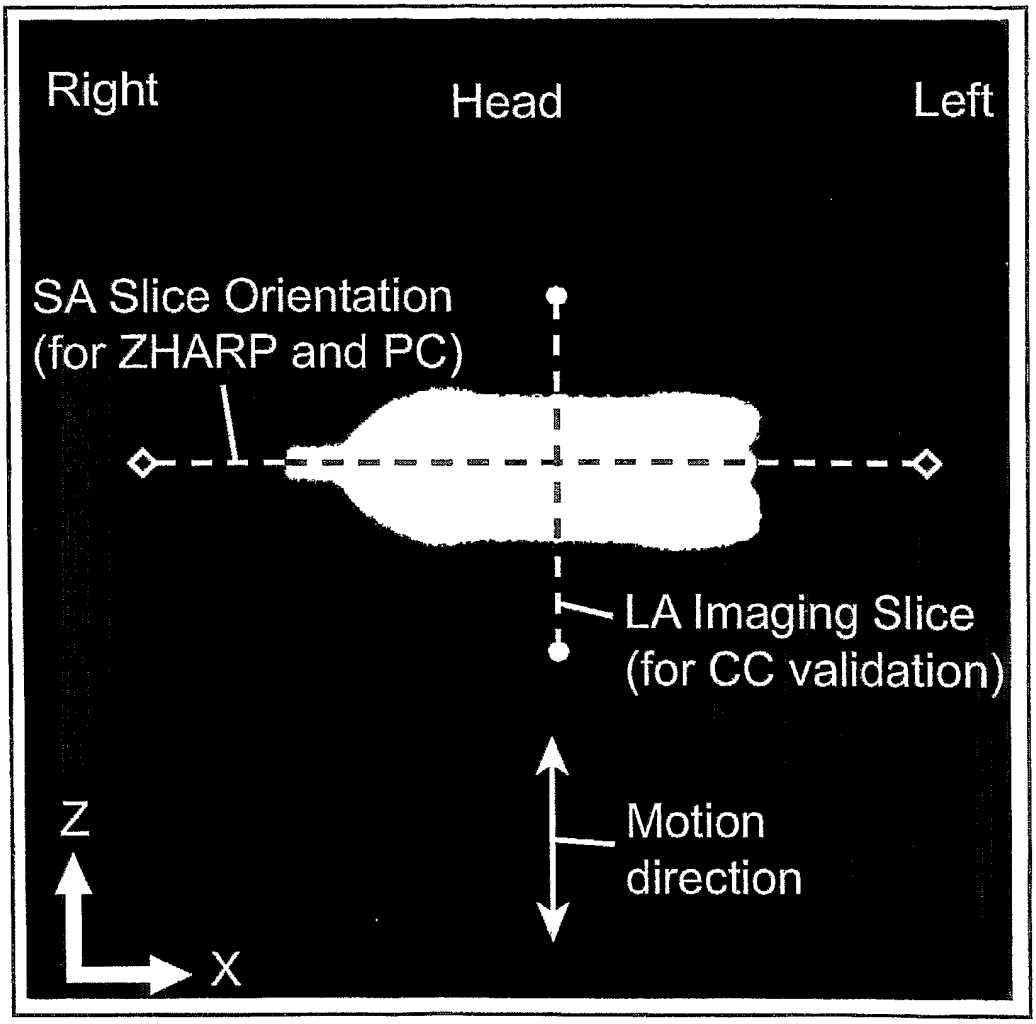

Right
Head
Left
SA Slice Orientation
(for ZHARP and PC)
LA Imaging Slice
(for CC validation)
Motion
direction
Z
X

FIG. 3

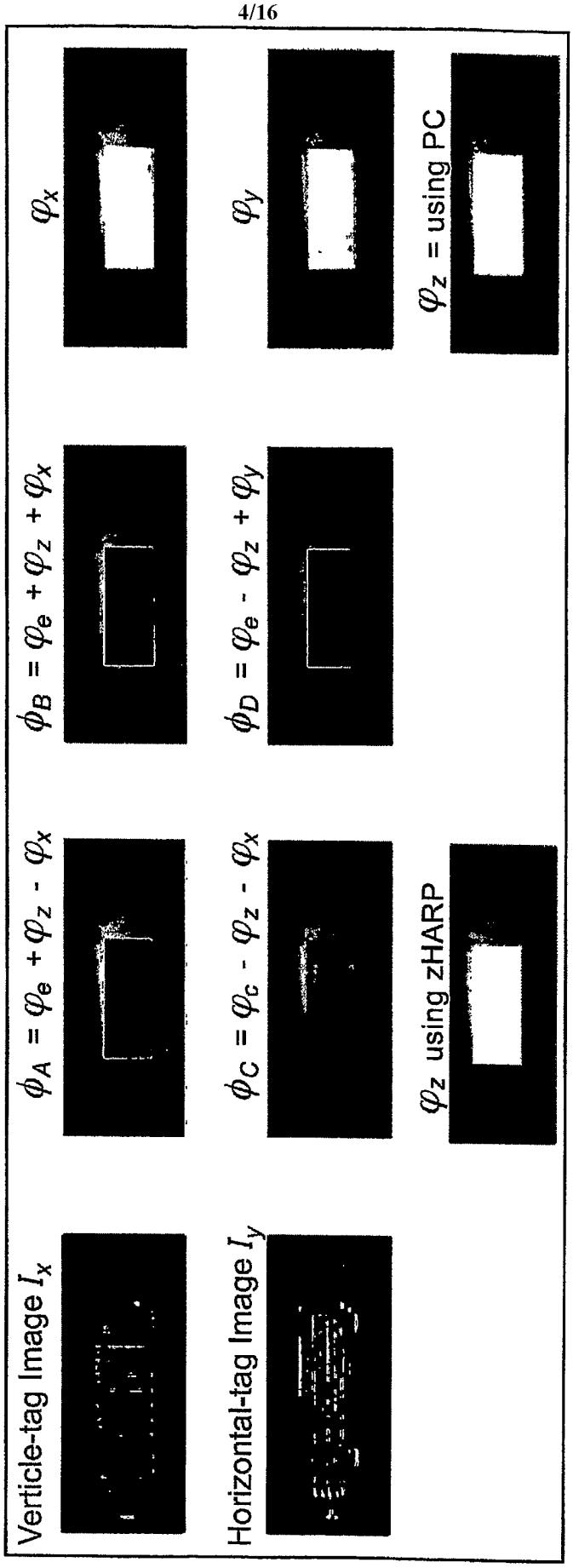

Verticle-tag Image I_x
$\phi_A = \varphi_e + \varphi_z - \varphi_x$
$\phi_B = \varphi_e + \varphi_z + \varphi_x$
φ_x
Horizontal-tag Image I_y
$\phi_C = \varphi_c - \varphi_z - \varphi_x$
$\phi_D = \varphi_e - \varphi_z + \varphi_y$
φ_y
φ_z using zHARP
φ_z = using PC

FIG. 4

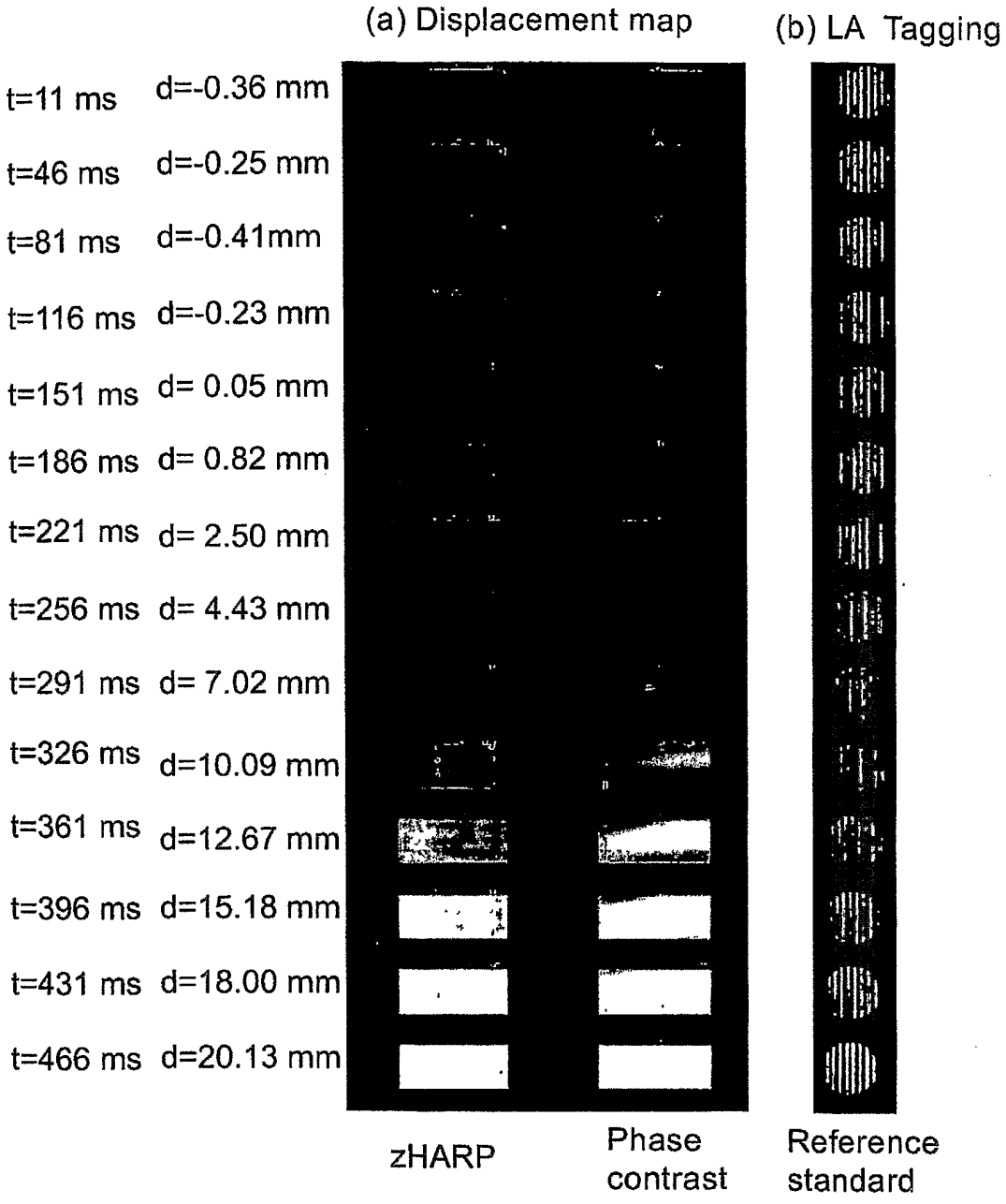

(a) Displacement map
(b) LA Tagging
t=11 ms d=-0.36 mm
t=46 ms d=-0.25 mm
t=81 ms d=-0.41mm
t=116 ms d=-0.23 mm
t=151 ms d= 0.05 mm
t=186 ms d= 0.82 mm
t=221 ms d= 2.50 mm
t=256 ms d= 4.43 mm
t=291 ms d= 7.02 mm
t=326 ms d=10.09 mm
t=361 ms d=12.67 mm
t=396 ms d=15.18 mm
t=431 ms d=18.00 mm
t=466 ms d=20.13 mm
zHARP
Phase contrast
Reference standard

FIG. 5

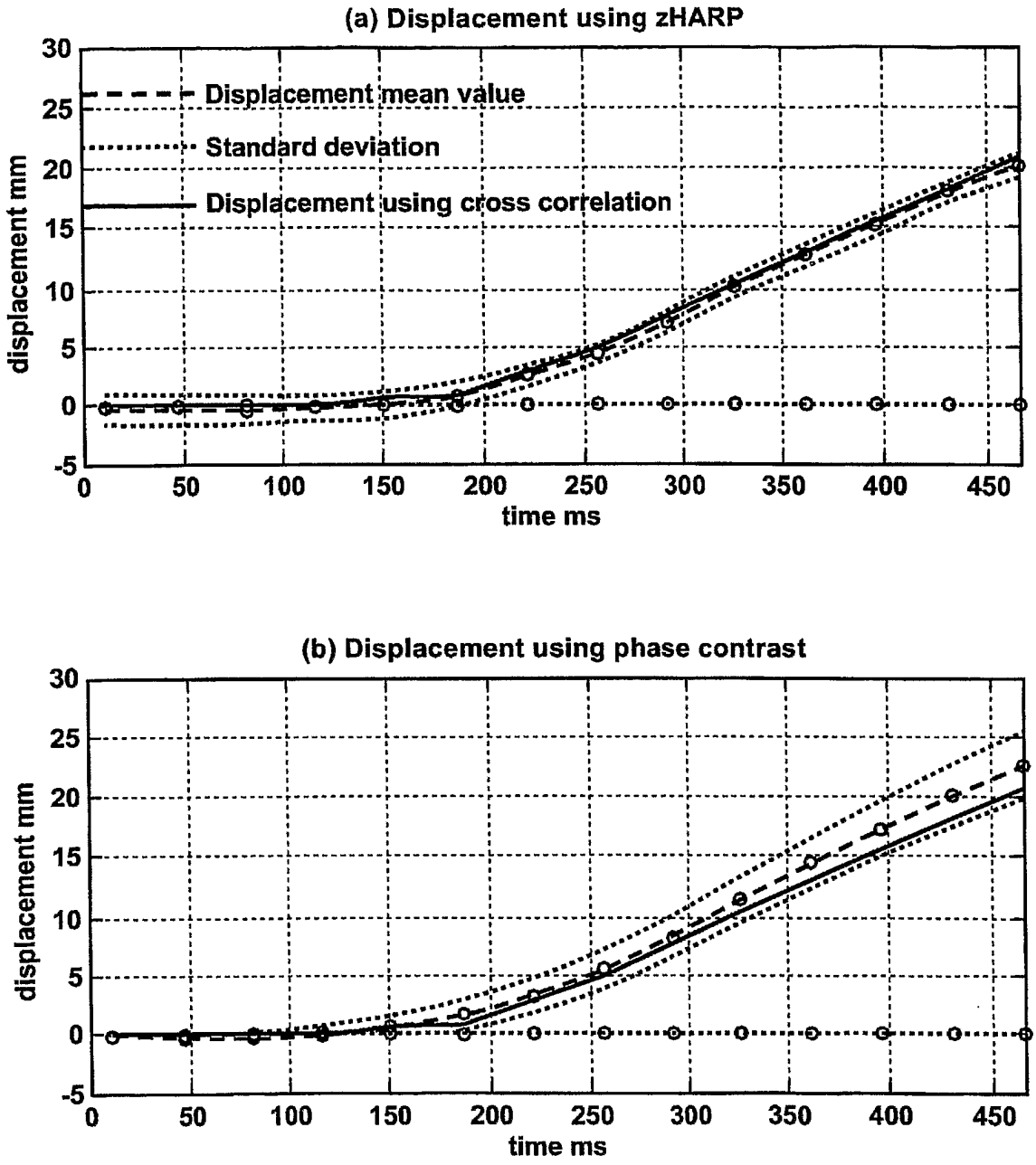

(a) Displacement using zHARP
Displacement mean value
Standard deviation
Displacement using cross correlation
displacement mm
time ms
30
25
20
15
10
5
0
-5
0
50
100
150
200
250
300
350
400
450
(b) Displacement using phase contrast
displacement mm
time ms

FIG. 6

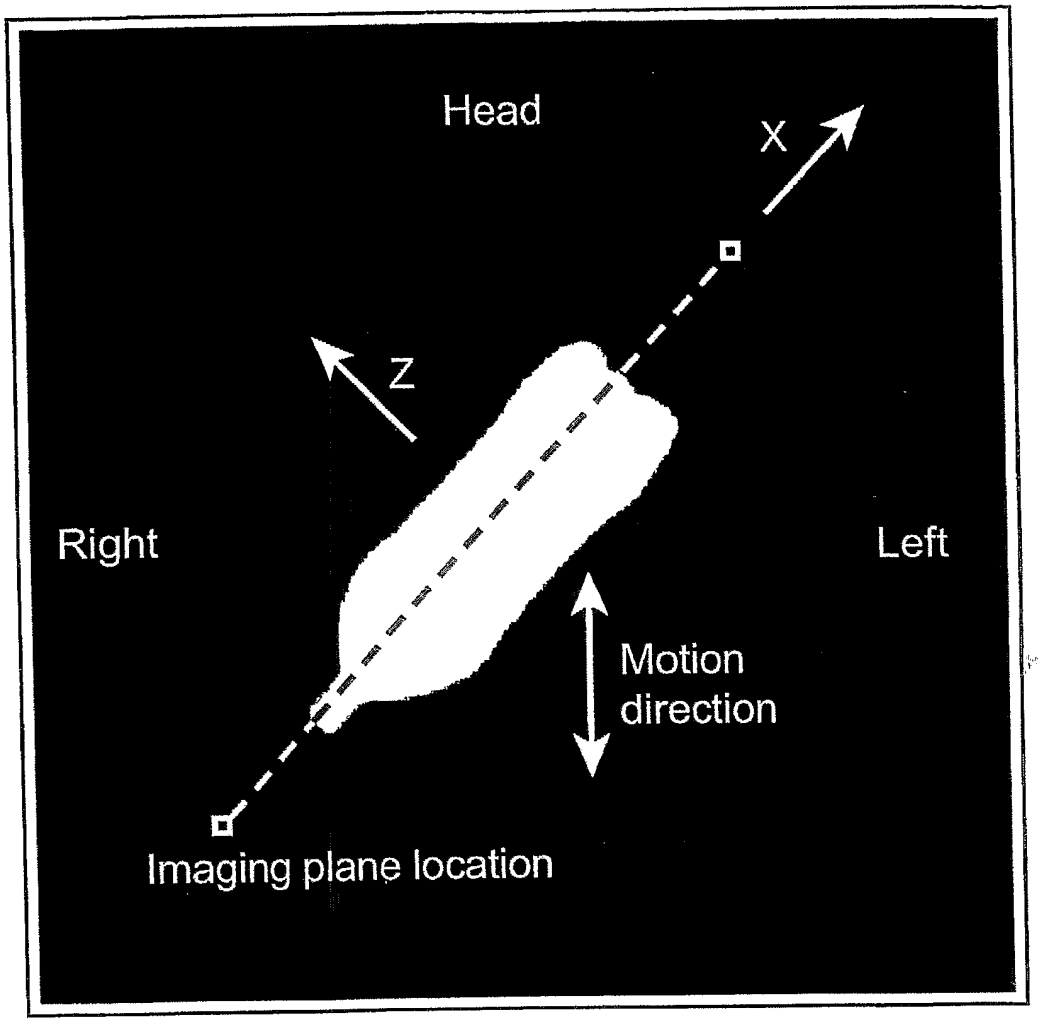

Head
X
Z
Right
Left
Motion
direction
Imaging plane location

FIG. 7

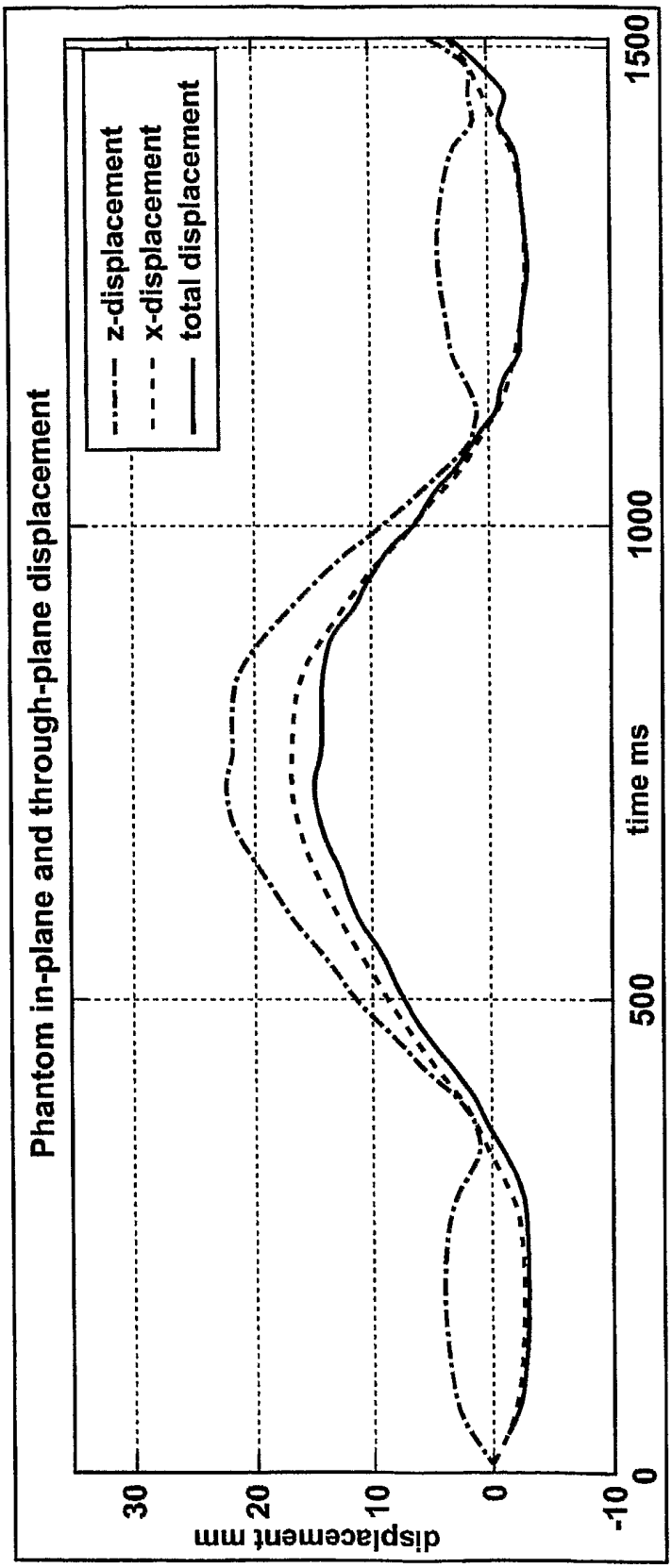

Phantom in-plane and through-plane displacement
z-displacement
x-displacement
total displacement
displacement mm
30
20
10
0
-10
0
500
1000
1500
time ms

FIG. 8

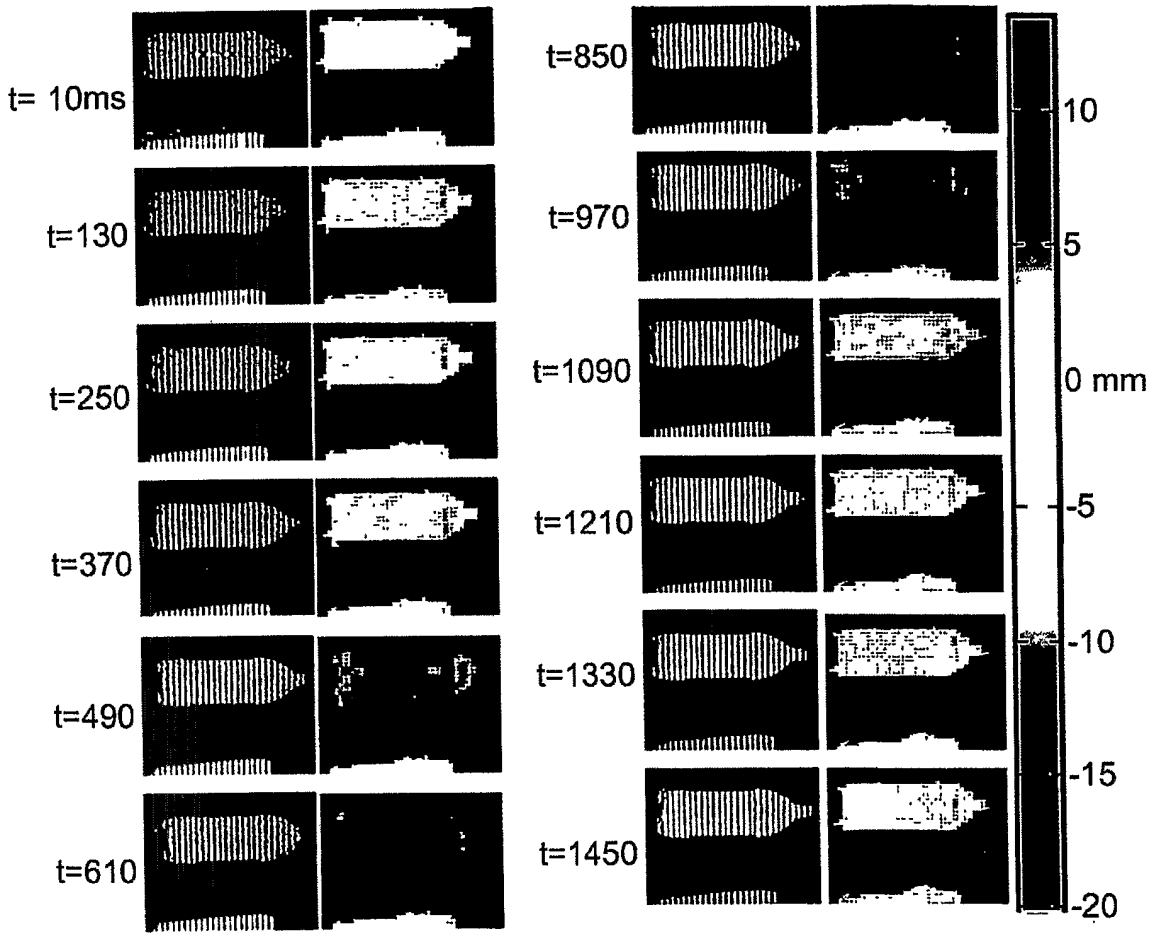

t= 10ms
t=130
t=250
t=370
t=490
t=610
t=850
t=970
t=1090
t=1210
t=1330
t=1450
10
5
0 mm
-5
-10
-15
-20

FIG. 9

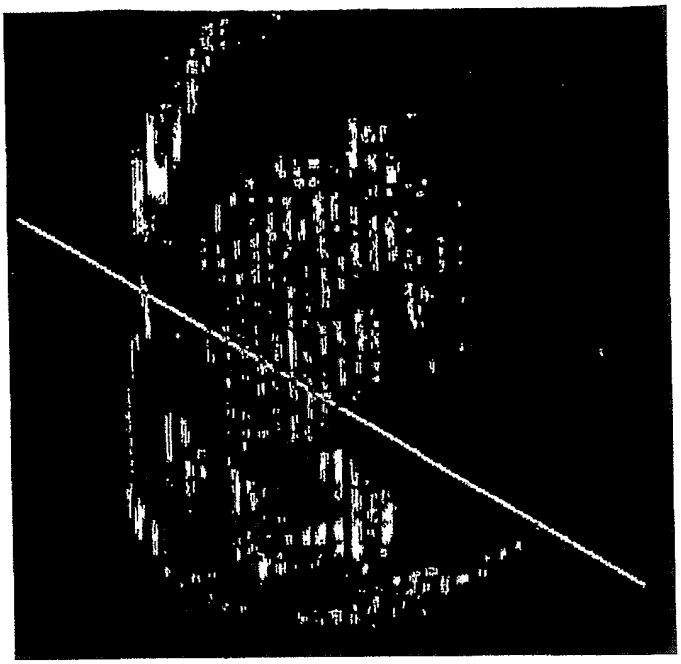


FIG. 10a

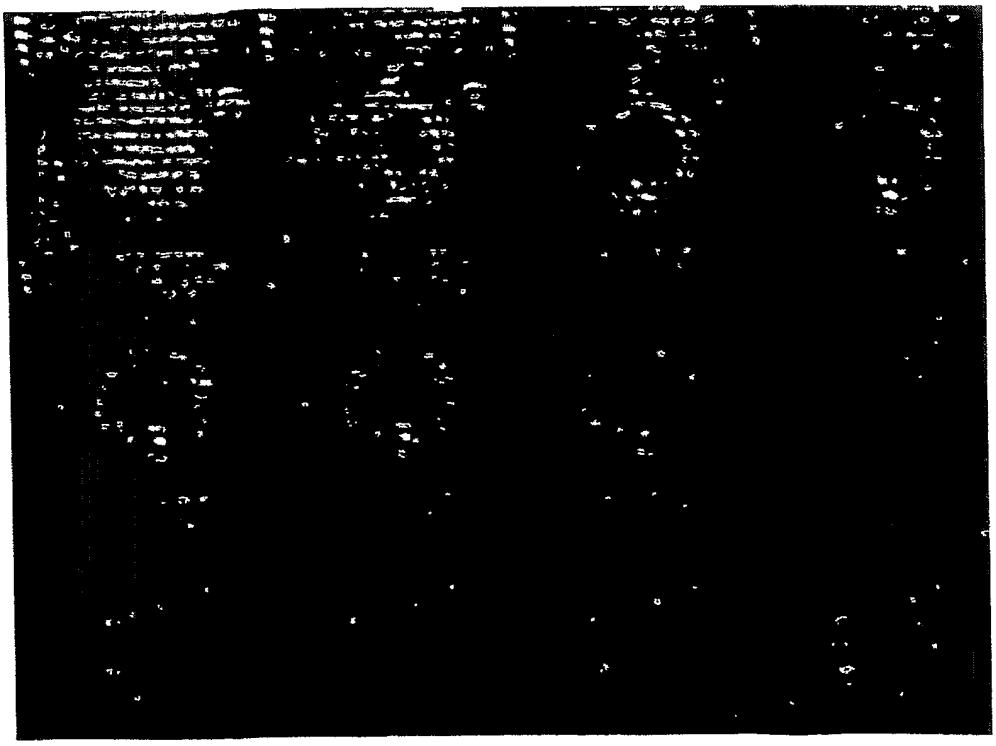


FIG. 10b

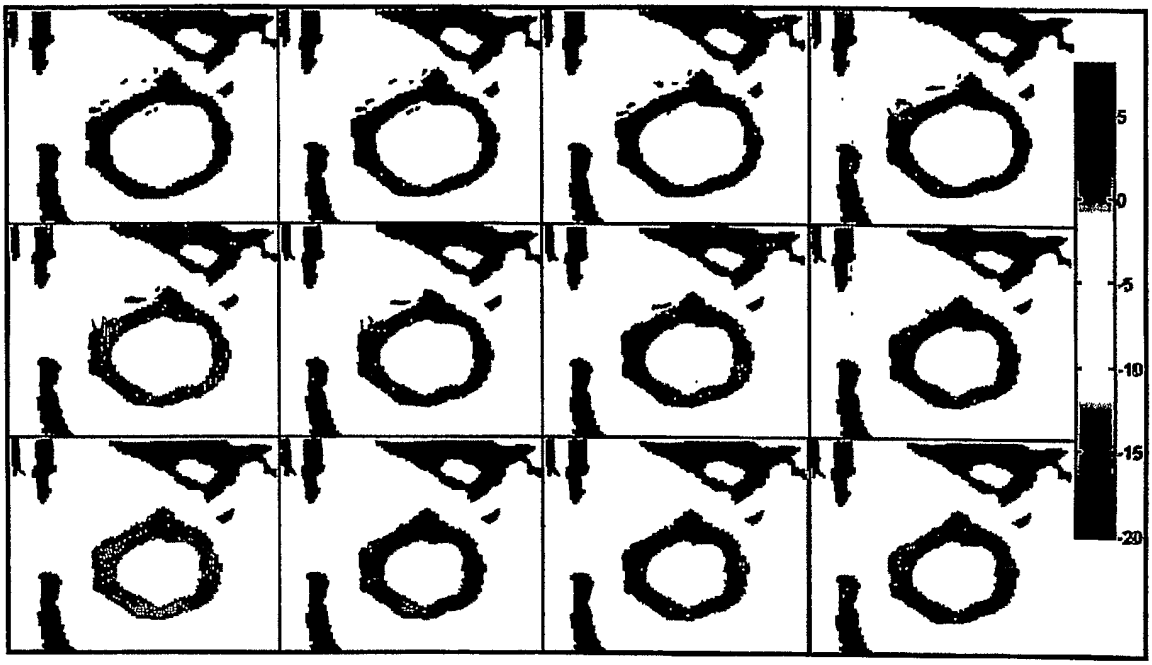


FIG. 11

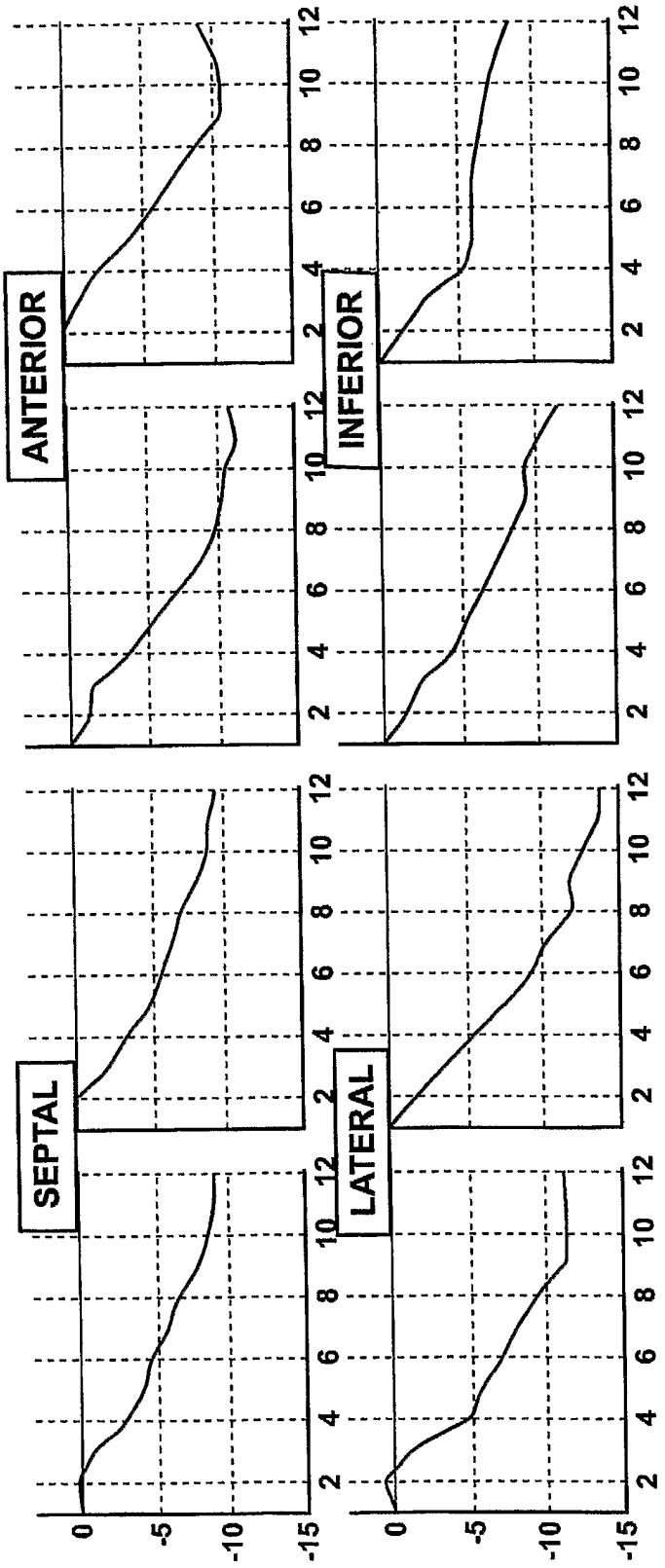
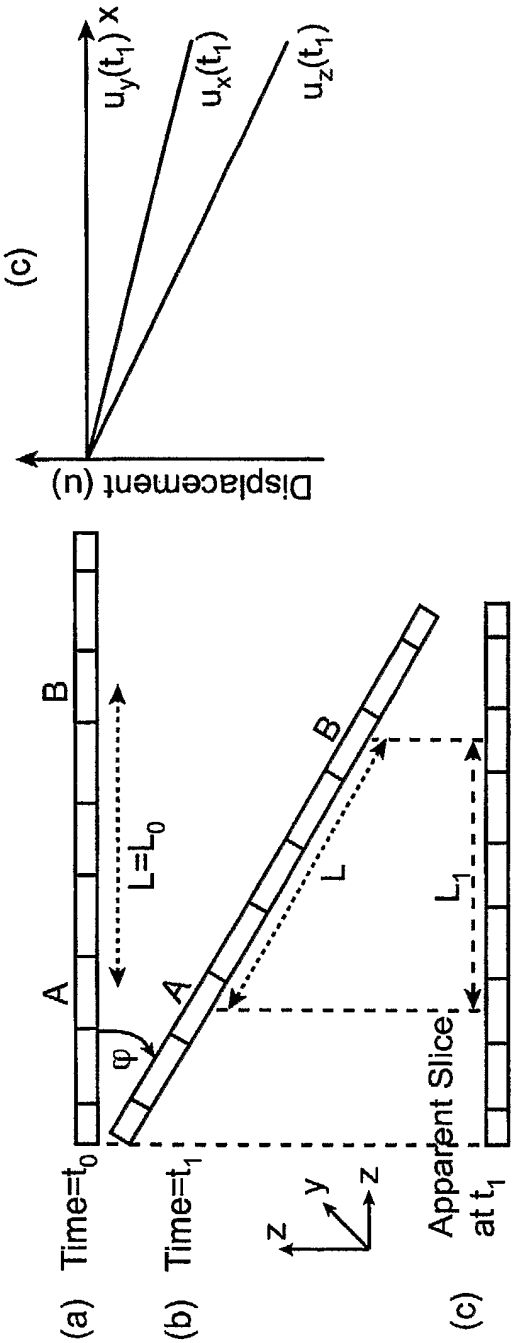


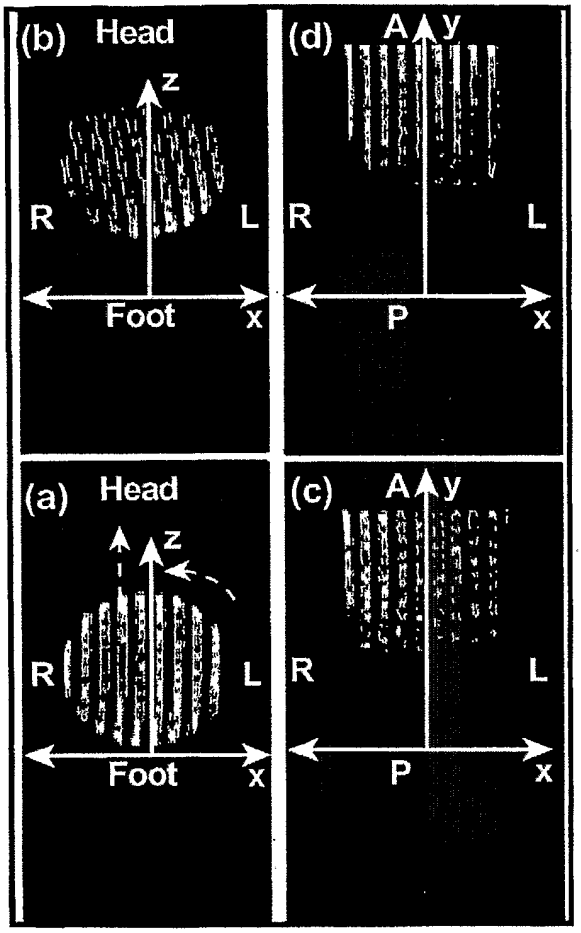
FIG. 12



An example of false apparent strain due to through-plane rotation φ.

(a) Original slice plane location at t_0. The length of the segment AB (L) is the same as the imaged length(L_0)
(b) True slice location at t_1. The segment AB has the same length.
(c) The imaged projection or the apparent slice. The imaged segment AB has a false length L_1. Apparent false strain= $(L_1-L_0)/L_0 = \cos(\varphi)-1$
(d) The components of the displacement vector (u) at t_1. At t_0 u=0. in SF-CSPAMM, only u_x and u_y can be computed.

FIG. 13



Setup of the cylindrical phantom experiment.

(a) The short axis (SA) original location at time = t_0. The object moves along the z-direction and rotates around the axis of symetry. Maximum z-displacement is 1". Max. rotation is 16°.

(b) SA slice location at t_1 after maximum displacement and rotation.

(c) The long-axis (LA) slice at t_0. Rotation and displacement are both through-plane.

(d) LA slice at t_1 with an apparent ~4%

Acquisition Window: 10ms

Spiral Interleaves: 20

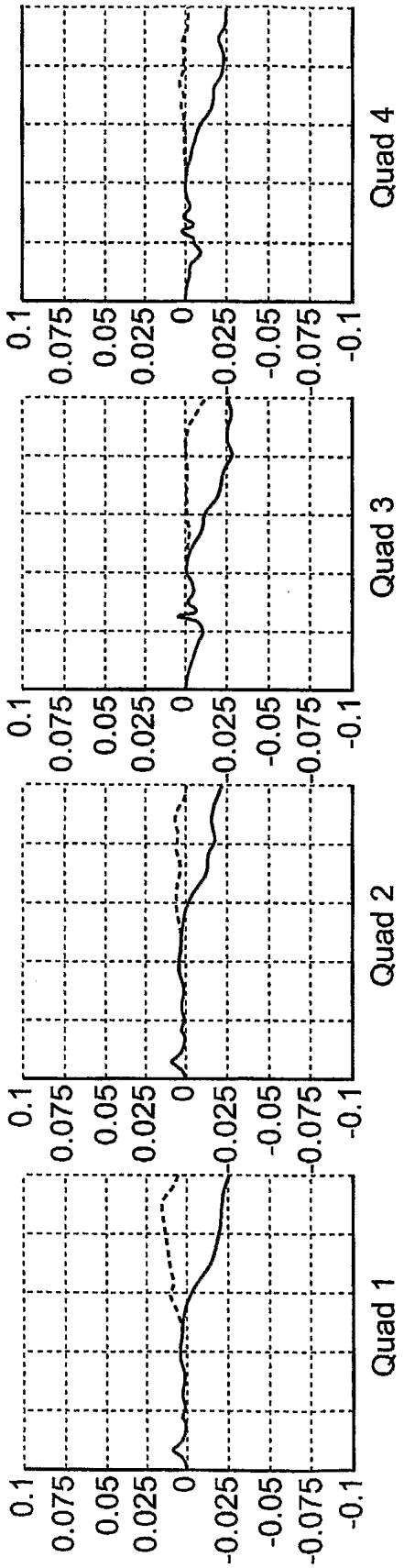
Res. 256x256,FOV 320mm

TE 1.1ms, TR 30ms

Slice Thickness 8mm

Tag-spacing 8mm

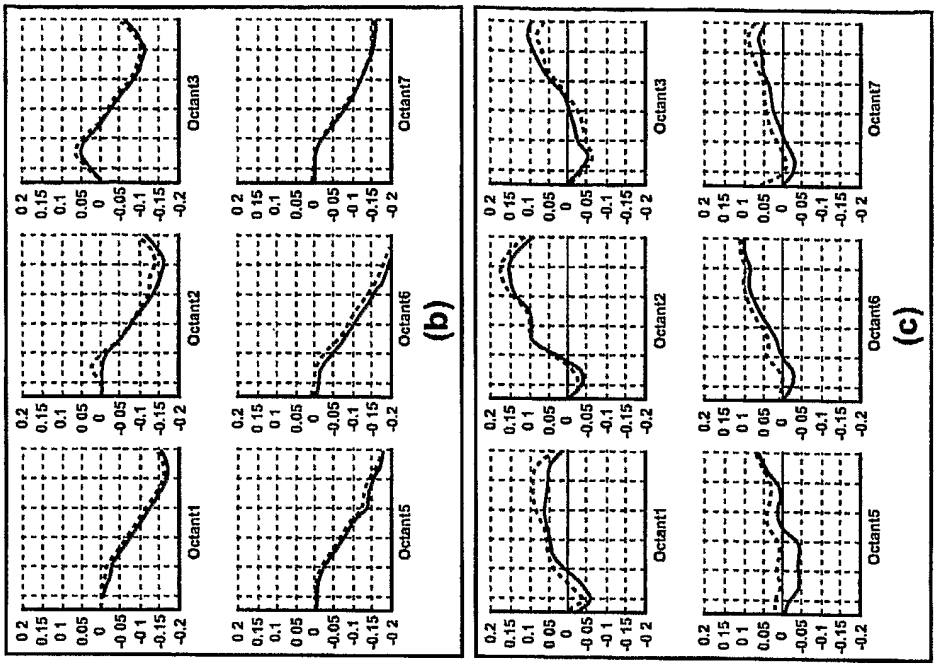
FIG. 14



Regional Eulerian Strain before and after correction

The LA slice is divided into four quadrants and the Eulerian strain is computed.
Green) Ignoring u_2 through-plane rotation not corrected. False strain of ~2% is apparent.
Red) Using u_2 to remove the effect of the through-plane rotation. Due to the vibration of the gel-phantom especially in the upper quadrants near the free surface. correction was not perfect.

FIG. 15



Human volunter equatorial SA slice. Segment Strain Comparison. Through-plane rotation adds false negative strain. True Ecc (compression) is less than the apparent Ecc, while True Err (thickening) is higher than the apparent Err.

(a) 8-Segments positions 1,2: Septal, 3,4: Interior, 5,6: Lateral, 7,8: Inferior.

(b) Ecc before correction (green) and after correction (red)

(c) Err before correction (green), and after correction (red).

Acquisition Window: 15ms. Spiral Interleaves: 12

Res. 256x256,FOV 350mm. TE 4.0ms, TR 30ms

Slice Thickness 6mm. Tag-spacing 8mm

FIG. 16